COMPARISON OF HEAVY ION- AND LASER-INDUCED SENSITIVE VOLUMES IN AN EPITAXIAL SILICON DIODE

By

Kaitlyn L. Ryder

Thesis

Submitted to the Faculty of the
Graduate School of Vanderbilt University
in partial fulfillment of the requirements
for the degree of

MASTER OF SCIENCE
in
ELECTRICAL ENGINEERING

September 30, 2019

Nashville, TN

Approved:

Robert A. Reed, Ph.D.
Brian D. Sierawski, Ph.D.

ACKNOWLEDGEMENTS

Science cannot be done alone, and so I would like to extend my heartfelt thanks to all of those who guided and supported me in making this work possible. Foremost I would like to thank my advisor, Robert Reed, for his guidance, patience, and enthusiasm for me and this work. Thanks is also due to many other members of the RER group at Vanderbilt: Ron Schrimpf, Sharon Weiss, Brian Sierawski, and Bob Weller for their instruction and expertise; Andrew Sternberg for his help in developing my experimental skills; Enxia Zhang for her amazing ability to bond any device; previous graduate students Isaak Samsel and Charlie Arutt for showing me the ropes and helping me feel confident in my abilities; and current graduate students Drew Tonigan, and Brandon Smith for many helpful discussions that helped propel this work forward. Dale McMorrow, Steve Buchner, and Ani Khachatrian at the Naval Research Laboratory were instrumental in preforming the laser experiments. Finally, I'd like to thank my husband and colleague, Landen Ryder, for his help and support and simulations. Without you this work, quite literally, could not have happened.

I would also like to extend my gratitude to my funding agencies, the Defense Threat Reduction Agency's basic research program and Sandia National Labs, for providing the funding to make this work possible.

TABLE OF CONTENTS

LIST OF FIGURES

CHAPTER I

INTRODUCTION

The single-event-effects sensitive volume model was first defined in [1] in order to relate the energy deposited in a sensitive volume by an ionizing radiation event to a circuit response. In order to enable on-orbit estimation of single event effects (SEE) rates, various versions of the sensitive volume model have been developed and used successfully. Early versions of sensitive volume models defined the sensitive volume geometry as a rectangular parallelepiped (RPP) [1], [2], and recent methods defined more complex sensitive volume geometries [3], [4] with multiple regions of different efficiencies. Experimentally-determined sensitive volumes are often used as inputs to error rate calculation simulators such as MRED [3], [4] and the CREME96 tool [5], [6]. The sensitive volumes are typically found using experimental data gathered at ground-based ion testing facilities. However, the cost and lack-of availability of these facilities has led to the need for a new characterization tool: the pulsed laser.

Pulsed laser SEE testing can be performed with either single-photon absorption (SPA) or two-photon absorption (TPA). SPA occurs when the wavelength of the laser has an energy greater than the bandgap of the target material. Here, a single photon is absorbed and leads to the creation of an electron-hole pair. TPA, on the other hand, occurs with wavelengths of energies less than the bandgap of the target material, and two photons are absorbed nearly simultaneously to create a single electron-hole pair. SPA- and TPA-induced SEE testing have their own set of pros and cons to be accounted for.

The intensity of SPA wavelength pulses is absorbed in a material exponentially according to Beer's Law. SPA-based SEE testing can provide good correlation to heavy ion testing results. However, the exponential decay of the intensity means that SPA-induced testing is limited to top-side irradiation of devices. This can be problematic with the increasing amounts of metallization that occurs on modern devices. TPA-induced SEE testing, on the other hand, is highly intensity dependent and relies on focused femtosecond pulsed lasers to achieve the intensities necessary for TPA to occur. The strong dependence of intensity on carrier generation allows the region of generated carriers to be locally confined and moved through a device by

changing the location of the laser focus. This allows for backside and through-substrate testing of devices. Both SPA- and TPA-based testing allow for areal scanning due to the small (~1 μm) spot size associated with focus lasers.

TPA-based testing is useful because of the refined spatial and temporal control of charge generation within devices, while offering increased availability and affordability compared to ion beams [7], [8], [9]. Recent research provides a theoretical and computational framework for quantitatively predicting TPA-induced SEE results [10], [11] empirical correlation of laser and ion results [12], [13], and a laser equivalent LET approach to correlate charge generated from pulsed lasers and ions [14]. However, it would be useful to develop a quantitative, predictive relationship between ion- and pulsed laser-induced SEEs without first empirically correlating laser and ion responses. A key, enabling metric towards this goal would be to define a common geometry for the sensitive volume generally useful for both ion- and laser-induced charge collection estimates.

In this work, a large area silicon diode fabricated on an epi-layer is used to study the similarities and differences between ion- and pulsed laser-induced collected charge sensitive volume geometries. A simple RPP structure sensitive volume is determined from collected charge measurements for both ion- and laser-induced collected charge at two different bias conditions. The ion- and laser-based sensitive volumes are used with ion LET curves and laser generated charge profiles to predict the collected charge for each of the charge deposition methods. These predicted collected charges are then compared with experimental results. While the ion- and laser-based sensitive volumes show good agreement with their own respective charge deposition methods, there are discrepancies when applied to the other charge deposition method. At the lower bias condition, the two sensitive volumes are different and show disagreement between the predicted amounts of collected charge, whereas at the higher bias condition the sensitive volumes are similar. The physical mechanisms responsible for the differences are discussed and limitations of quantitative ion-laser SEE measurements are considered.

CHAPTER II

BACKGROUND

II.1 Heavy Ion-Induced Collected Charge Sensitive Volume Definition

A sensitive volume is a region within a device such that when charge is deposited, a response occurs. In this work, the response that is being examined is the collected charge observed from a single event transient (SET) after charge is deposited either from a heavy ion or a pulsed laser. The ion-induced collected charge sensitive volume for this device is motivated by the relationship between energy deposited and charge generated by an ion:

$$Q_{coll} = \frac{q\,\rho}{E_{ehp}} \int_0^{SD_{ion}} LET(z)\,dz \qquad (II.1)$$

where ρ is the density of the target material, E_{ehp} is the energy required to create an electron-hole pair in the target material (3.6 eV/ehp in Si) and *LET(z)* is the linear energy transfer, defined as:

$$LET(z) = -\frac{1}{\rho}\frac{dE_{elec}(z)}{dz} \qquad (II.2)$$

in traditional units of MeV-cm^2/mg. $\frac{dE_{elec}}{dx}$ is the rate of change of the electronic stopping energy of the ion as it passes through a material. Combining these two equations results in the relationship:

$$Q_{coll} = \frac{q}{E_{ehp}} \int_0^{SD_{ion}} \frac{dE_{elec}(z)}{dz}\,dz. \qquad (II.3)$$

Therefore, collected charge is related to the rate of electronic energy lost by an ion to the surrounding material and the path length over which that energy is lost. This path length, SD_{ion}, is

the sensitive volume depth. Because of the large scale nature and symmetry of the test device in this work, the sensitive volume thickness is the only unknown aspect of the sensitive volume. The integral here runs from the surface of the device to the sensitive volume depth, which is supported by TCAD simulations, but that is not true for all devices and should not be taken as a universal truth.

Equation 1 assumes a charge collection efficiency of 100%, and can be used to directly solve for the sensitive volume thickness by integrating the LET curve over a path length until the integrated charge is equal to the collected charge. Figure II.1 [15] demonstrates this. On the left is the LET curve for 1.3 GeV Xe as it passes through Si; it has a surface LET of 59 MeV-cm^2/mg and the LET increases by 10% over the first 40 μm in Si. The figure on the right shows the integrated LET curve and its intersection with the experimentally determined collected charge of 11 pC. Using Equation 1 results in a path length of approximately 13.5 μm necessary for the integrated LET curve to have the same charge as that seen experimentally. This would then be the ion-based sensitive volume, SD_{ion}.

It should be noted that 100% collection efficiency does not have to be true. A device structure could have efficiencies greater than or less than 1 depending on the particular physical processes at play. In those cases, a multiplier exists in front of the integral that represents the collection efficiency [3], [4], [16].

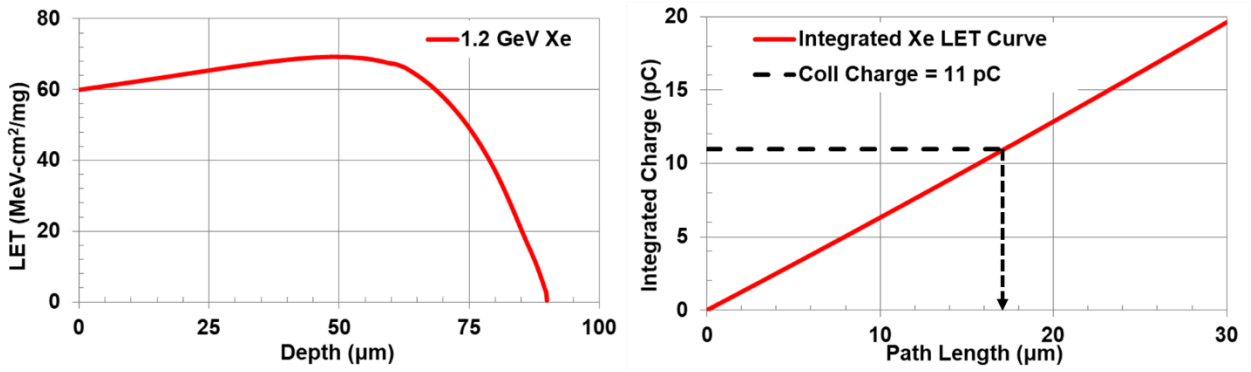

Figure II.1. LET curve as a function of depth into Si for a 1.2 GeV Xe ion (left). Integrated Xe LET curve (red) and its intersection with the experimental collected charge 11 pC (black) (right).

II.2 Description of Two-Photon Absorption Mechanisms

Two-photon absorption (TPA) is a nonlinear optics process in which two photons are absorbed nearly simultaneously, resulting in the creation of a single electron-hole pair, see Figure II.2. The nearly simultaneous absorption of photons is achieved through virtual states that result from defects. The first photon is absorbed and excites an electron into the virtual state; a second photon is then absorbed at nearly the same instant and causes the electron to be excited from the virtual state into the conduction band. Carrier generation as a result of TPA can be described by the following coupled differential equations:

$$\frac{dI(r,z)}{dz} = -\alpha_0\, I(r,z) - \beta_2\, I^2(r,z) - \sigma_{FCA}\, N(r,z)\, I(r,z) \qquad (II.4)$$

$$\frac{d\Phi(r,z)}{dz} = k_0\, n_0 + k_0 \left(n_2\, I(r,z,t) + \Delta n_{FCR}\, N(r,z,t)\right) \qquad (II.5)$$

$$\frac{dN(r,z)}{dt} = \frac{\alpha_0}{\hbar\omega} I(r,z) + \frac{\beta_2}{2\hbar\omega} I^2(r,z) - \frac{1}{\tau} N(r,z,t) \qquad (II.6)$$

where I is the intensity, α_0 is the linear absorption coefficient, β_2 is the TPA absorption coefficient, σ_{FCA} is the coefficient of free carrier absorption, N is the number of free carriers, Φ is the phase of the light, k_0 is the vacuum wave vector ($2\pi/\lambda$), n_0 is the refractive index at that wavelength, n_2 is the Kerr coefficient, Δn_{FCR} is the change in refractive index due to free-carrier refraction, and $\hbar\omega$ is the photon energy.

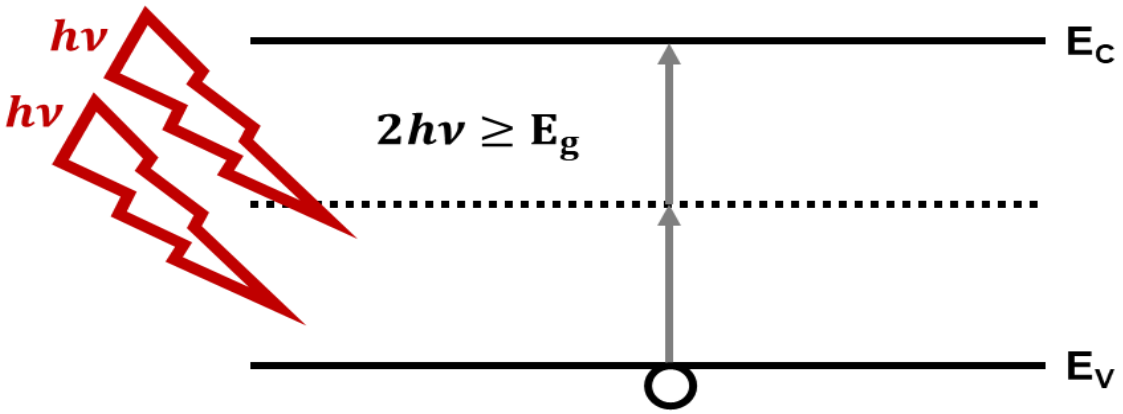

Figure II. 2. TPA occurs when two photons whose sum of energies is greater than the bandgap are nearly simultaneously absorbed leading to the generation of one electron-hole pair through a virtual state.

Because TPA requires nearly simultaneous absorption of two photons, it only occurs in regions of high photon intensity. As such, femtosecond pulsed lasers are necessary for achieving the intensities necessary for TPA to be possible. Figure II.4 shows three time-integrated charge generated profiles that result from solving Equations II.4-6 when a 990 pJ laser is focused at locations 0 μm, 17.5 μm, and 24 μm into the Si diode used as a test structure in this work (described in more detail in III.1). The intensity dependence of TPA can be seen as charge is mainly generated only in the region directly around the focus of the laser pulsed. This localized generation of carriers gives TPA-induced SEE investigations flexibility over ion-based investigations. Because photons are only absorbed in the region near the laser focus, the region of charge generation can be arbitrarily moved throughout a device. This allows for backside illumination of devices, a necessity as the front-end of line processing becomes more complicated with more metal layers [7], [17].

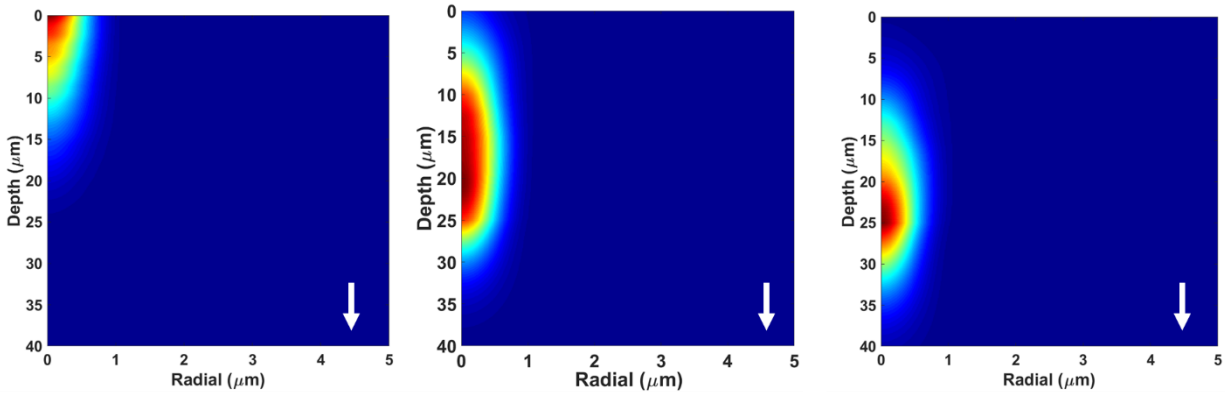

Figure II. 3. Time-integrated charge generated distributions that result from solving the couple differential equations for the propagation of light for a 990 pJ focused pulsed laser at focal positions of 0 μm (left), 17.5 μm (center), and 24 μm (right).

II.3 Laser-Induced Collected Charge Sensitive Volume Definition

A laser-induced collected charge sensitive volume can be defined in a similar manner to the ion-based sensitive volume by relating the generated charge to the collected charge. Unlike the ion-based sensitive volume with the LET curves, laser-generated charge can have a non-uniform areal distribution, so the necessary integral is a volume integral:

$$Q_{coll} = \iiint_{V=A\,SD_{laser}} \frac{dQ_{gen}(V)}{dV} dV. \qquad (II.7)$$

The laser-based sensitive volume is a combination of the area, A, and path length, SD_{laser}, necessary to integrate the generated charge over to see the experimentally observed collected charge. As with ions, a non-unity collection efficiency can be added to this equation by a scaling factor in front of the integral. This equation is time independent and assumes that all of the charge generation is done on a time scale much faster than charge collection so the two processes can be examined independently; this same assumption is made for ions as well.

Finding the time-integrated generation rate for any given pulsed laser experiment requires solving the couple differential Equations 4-6 and knowing the particulars of the laser pulsed, such as length, spot size, and wavelength. An optical simulation tool, such as Lumerical [18], can then be used to solve for the time-integrated generated charge distributions. Lumerical is an FDTD nanophotonic simulation software package that captures optical and nanophotonic effects through a three-dimensional solution of Maxwell's Equations. It has been modified to consider charge generation as described in Equations II.4-6 so that TPA-induced SEE simulations can be performed [19]. Lumerical's output is time-integrated generated charge distributions, such as those seen in Figure II.3, which can be examined independently or ported into Sentaurus TCAD for transient simulations.

Once the charge generated distributions are known, solving for a laser-based sensitive volume follows the same procedure as that for an ion-based sensitive volume. First, the radial part of the carrier distributions is integrated to create a line curve of charge generated per unit depth. The entire radial distribution is integrated due to the large scale nature of the test structure used here. The line curve is then integrated until the integrated charge is equal to the experimentally observed collected charge. The path length at which the integrated charge equals the collected charge is the sensitive volume depth. This process is shown in Figure II.4 using the TPA charge generated distribution given in the center panel of Figure II.3. The left panel shows the line curve that results from integrating the radial portion of the charge generated distribution, and the right panel shows the integrated charge and where it intersects with the experimental collected charge of 14 pC. The sensitive volume thickness is found to be 21.4 μm for this particular focal position and pulsed energy.

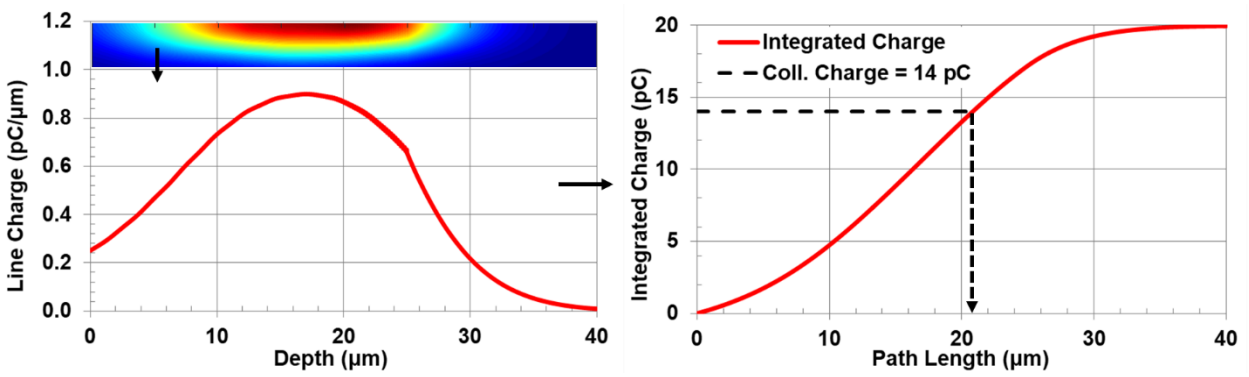

Figure II. 4. Charge generated distribution and line charge generated curve (left) and integrated charge curve (right) for the example charge generated distribution shown in Figure II.3.

CHAPTER III

EXPERIMENTAL SET-UP AND PROCEDURES

III.1 Test Structure

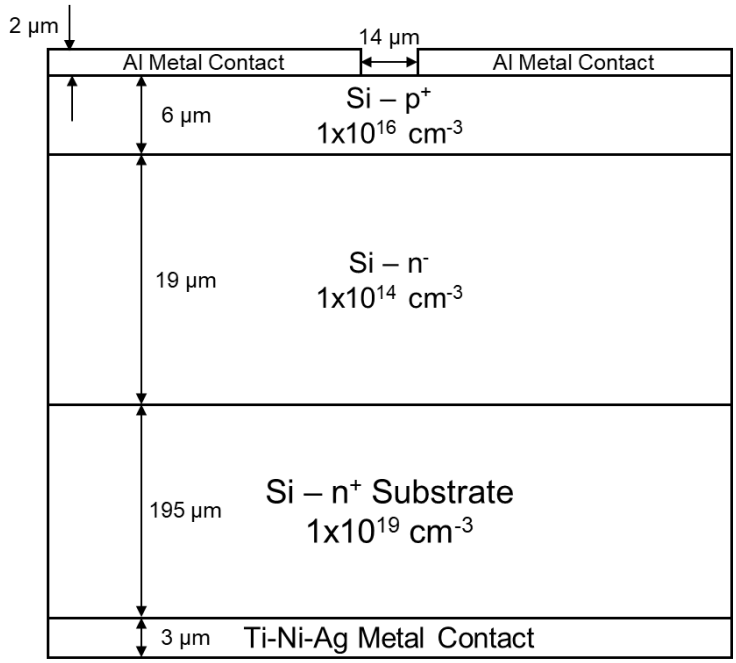

Figure III. 1. Cross section of diode test structure. The diode is 1.82 mm^2 and 220 µm thick.

An epitaxial silicon diode manufactured by Beijing Microelectronics Technology Institute (BMTI) was used as a test structure in this work. A cross section of the diode can be seen in Figure III.1. The devices were manufactured with 196 μm^2 holes in the top Al metal contact, allowing for top-side illumination of the junction. The area of the metal holes accounts for less than 0.1% of the total area of the top contact, so electrical performance is not affected by their presence. It should be note that the holes in the metallization are small enough to perturb the laser profile as it passes through it, so effects resulting from the optical perturbations are accounted for in the optical simulations. The diode was reversed biased at 5 V and 90 V for all sets of

experiments, resulting in depletion region widths of 5 μm and 14.5 μm, respectively, which forms mainly in the n^- region.

III.2 Experimental Setup

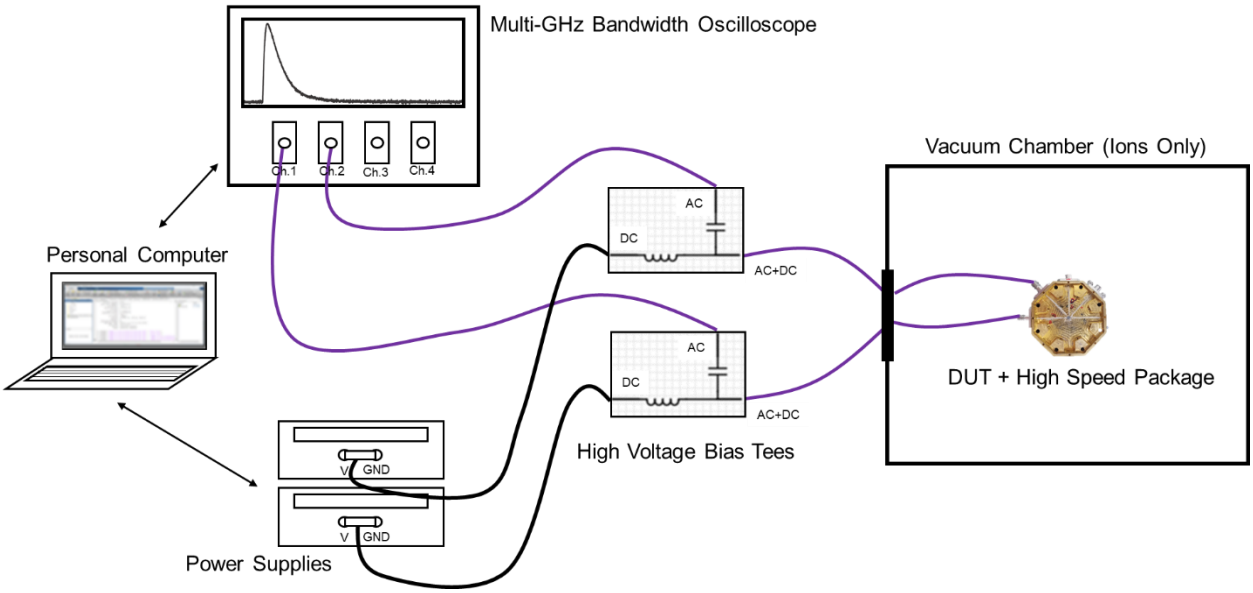

Figure III. 2. Experimental setup used for heavy ion and pulsed laser experiments. The same high speed packages, bias tees, and high speed cables were used for all experiments.

Figure III.2 is a diagram of the experimental setup used for all of the testing reported here. Heavy ion testing was performed at Lawrence Berkeley National Lab's (LBNL) 88" Cyclotron and pulsed laser testing was performed at the Naval Research Laboratory (NRL) Ultrafast Laser Facility. The diode is mounted on a custom-milled high speed package with microstrip transmission lines and precision 2.92 mm K-connectors. Gold bond wires connect the diode contacts to the transmission lines, which are connected to 40 GHz K-connectors. Gore 40 GHz high speed cables connect to the high speed package [20], [21]. Heavy ion experiments were performed in vacuum, so the high speed cables connect to an SMA feedthrough and then to more high speed cables outside of the vacuum chamber. The high speed cables connect to 12.5 GHz Tektronix bias tees that are rated to 200 V_{DC} bias. More high speed cables connect the AC side of the bias tees to a high speed oscilloscope, while BNC cables connect the DC side of the bias tees to the power supply. For heavy ion experiments, a 12.5 GHz single shot Tektronix oscilloscope was used to observe and record transients; a 16 GHz single shot Tektronix oscilloscope was used

for laser experiments performed at NRL. Keithley 2410s were used as the power supply at LBNL and Keithley 2400s were used at NRL. A personal computer is used to record and analyze the transients observed.

LBNL's 10 MeV/u ion cocktail was used, and a range of LETs and biases were examined during heavy ion experiments. The list of ions used is shown in Table III.1 [22]. Because of the broad beam nature of LBNL's ion beam, a pin hole was used to ensure that ions only struck the center of the device to prevent problems associated with edge effects. The pinhole, shown in Figure III.3, was made of 100 μm thick stainless steel and was 200 μm in diameter. It was visually aligned over the center of the diode using an optical microscope. An aluminum mount, Figure III.3 (right panel), was used to attach the pinhole to the top of the high speed package. For each ion and bias condition, 10,000 SETs were recorded for analysis.

TABLE III.1 LBNL HEAVY IONS

Ion	Energy (MeV)	Surface Incident LET (MeV-cm^2/mg)	Range in Si (μm)	Range in Stainless Steel (μm)
Xe	1200	59	90	35
Cu	660	21	108	41
Si	290	6	54	54

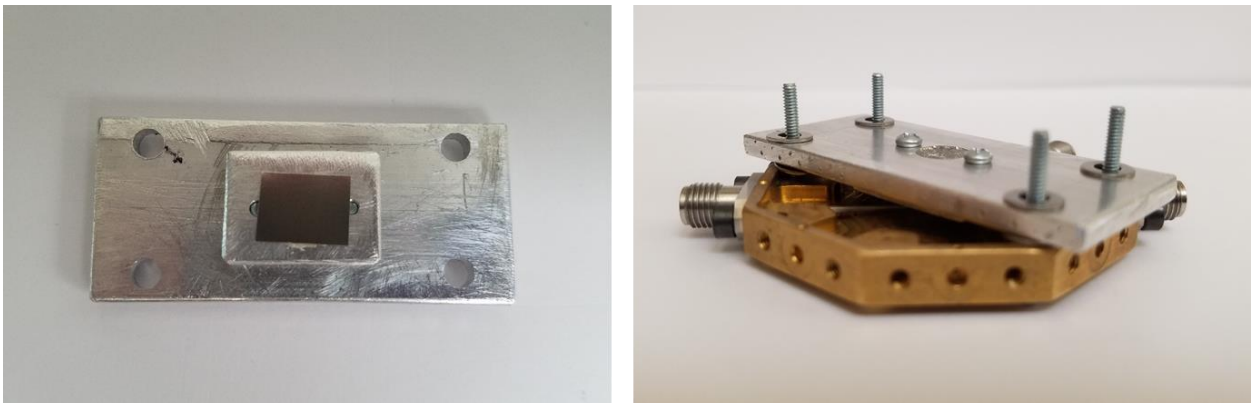

Figure III. 3. Top view (left) and side view (right) of the stainless steel pinhole and aluminum mount used during heavy ion experiments at LBNL.

Pulsed laser testing at NRL was performed using a Ti:Sapphire tunable optical parametric amplifier (OPA) tuned to a wavelength of 1260 nm. This wavelength carries an energy of 0.98 eV,

which is less than silicon's bandgap energy of 1.12 eV but greater than half the bandgap, allowing for TPA. Detailed descriptions of the laser setup and dosimetry at NRL are available in [23]. The FWHM spot size and FWHM temporal width of the laser pulsed was 1.36 μm and 130 fs, respectively. Pulsed energies of 400 pJ, 750 pJ, and 990 pJ were used. A series of measurements made by changing the depth of the laser focus within a device, called a depth scan, was performed at each pulsed energy and bias condition. At each focal position, 200 SETs were recorded for analysis.

III.3 Data Analysis

In order to ensure equivalent analysis between experiments, the same analysis procedure was applied to all data sets. The double exponential fitting function:

$$f(t) = \begin{cases} A + Bt, & t < t_{on} \\ A + Bt + I\left(e^{\tau_1(t-t_{on})} - e^{-\tau_2(t-t_{on})}\right), & t \geq t_{on} \end{cases}, \quad (III.1)$$

was applied to each recorded transient. A and B are parameters used to quantify the noise level, t_{on} is the time at which the transient starts and is determined by the horizontal offset on the oscilloscope, I is proportional to the peak amplitude of the transient, and τ_1 and τ_2 are time constants relating to the rise and fall times of the transient. Figure III.4 shows an ion- and laser-induced transient along with the fitting function associated with those particular transients. As can be seen, the fitting function provides good agreement with the overall shape and magnitude of the transients while reducing the impact of measurement noise. The fitting function also allows for double transients from ion-based experiments to be filtered out.

Once a fitting function has been defined for a particular transient, it can be analyzed to find the collected charge of the individual transients by integrating using the trapezoidal method:

$$\int f(x)dx = \sum_{i=0}^{N-1} \frac{f(x_i) + f(x_{i+1})}{2}(x_{i+1} - x_i). \quad (III.2)$$

The area of the noise components of the transient is also calculated using the trapezoidal method and is subtracted from the overall integral, resulting in the integral of just the transient. This

integral is equivalent to the total collected charge in picocoulombs if the units of time are nanoseconds and the magnitude is milliamps. The collected charge for each transient is recorded, and statistics for each experiment can be analyzed.

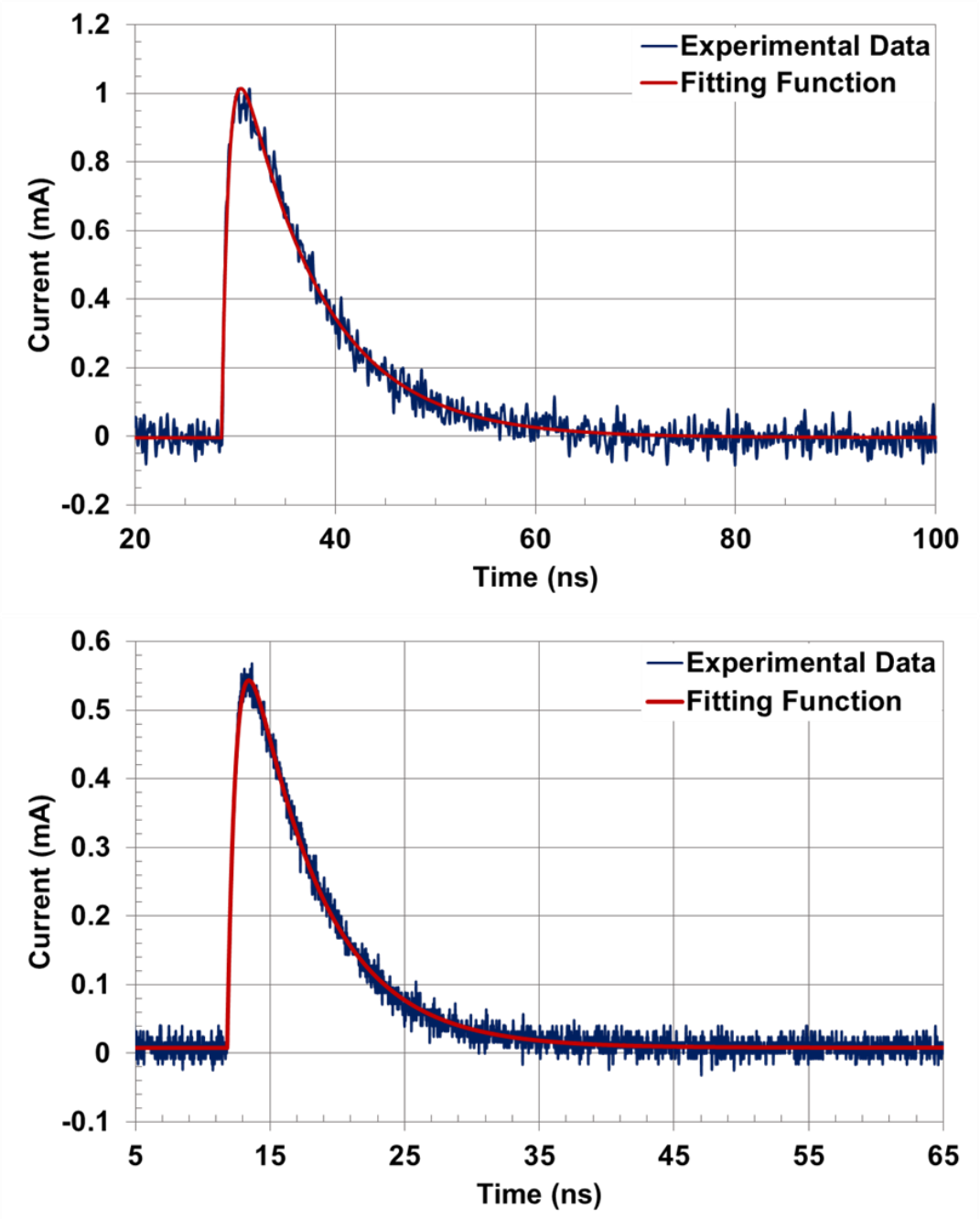

Figure III. 4. An ion-induced (top) and laser-induced (bottom) SET and its corresponding fitting function. The fitting function for both types of SETs captures to overall shape of the transient response while limiting the effect of noise on future analysis.

CHAPTER IV

HEAVY IONS: EXPERIMENTAL RESULTS AND SENSITIVE VOLUMES

Figure IV.1 shows the results from the heavy ion experiments at reverse biases of 5 V and 90 V. The results are as expected for long range ions: the collected charge increases approximately linearly with incident LET at a rate of 0.17 pC/MeV-cm^2/mg and 0.27 pC/MeV-cm^2/mg for -5 V and -90 V, respectively. The error bars are one standard deviation from the mean for each experiment from 10,000 recorded SETs, and are within 25% of the mean. These experimentally observed collected charges were used together with the LET curves for each ion, shown in Figure IV.2 [15], to find the ion-induced sensitive volume, SD_{ion}, according to Equation II.1. A summary of the sensitive volumes can be found in Table IV.1.

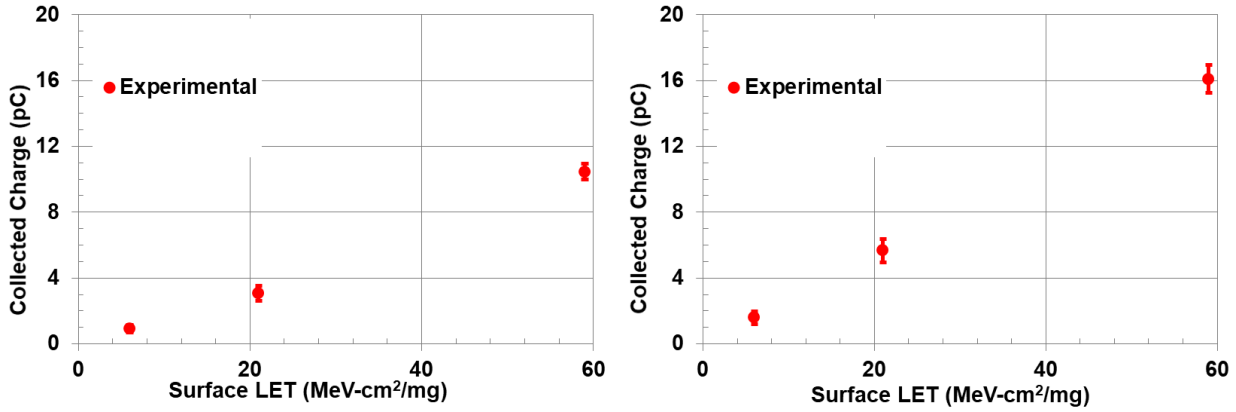

Figure IV. 1. Ion collected charge experimental results for biases of -5 V (left) and -90 V (right). The error bars show one standard deviation from the mean, given 10,000 SETs.

Taking the average of the sensitive volumes for each bias, 14.7 µm (-5 V) and 24.6 µm (-90 V), gives a sensitive volume for each bias condition. The average sensitive volume is used for the singular ion-based sensitive volume to account for experimental variation due to contamination in the ion beam, noise fluctuations, and experimental error. The SD_{ion} + LET Curves points in Figure IV.3 shows the collected charge predicted by integrating the ion LET curves using the ion-induced sensitive volume according to Equation II.1. Overall, the average ion-induced sensitive volume predictions are consistent with the results observed experimentally and deviate from the

experimental average by no more than 12%. The rate of charge collection from the ion-induced sensitive volume predictions are slightly less than that for the experimental results for both biases: 0.16 pC/MeV-cm^2/mg and 0.26 pC/MeV-cm^2/mg for -5 V and -90 V, respectively.

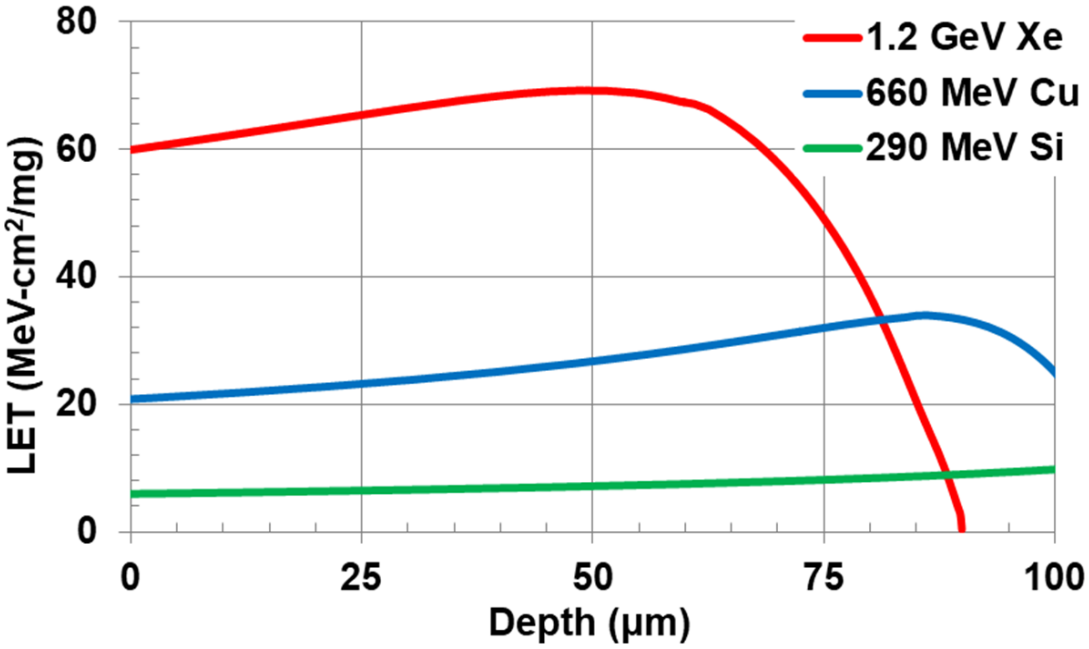

Figure IV. 2. LET curves calculated from SRIM for each of the ions used for testing over 100 µm in Si.

TABLE IV.1 ION-INDUCED SENSITIVE VOLUMES

Ion	Bias (V)	Avg. Collected Charge (pC)	Sensitive Volume (µm)
Xe	-5	10.5	16.7
Cu	-5	3.08	13.5
Si	-5	0.91	14
Xe	-90	15.9	25.1
Cu	-90	5.67	24.3
Si	-90	1.6	24.2

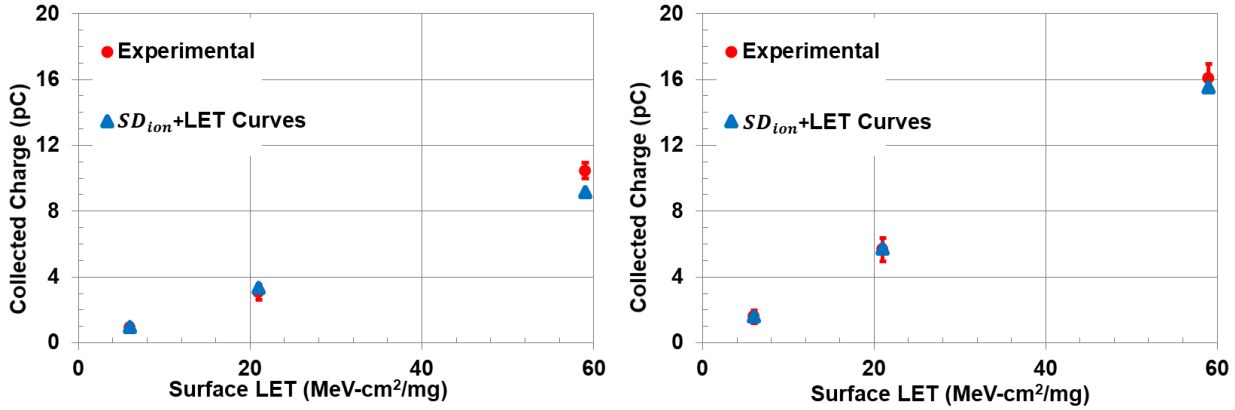

Figure IV. 3. Experimental (red circles) and ion-induced sensitive volume (blue triangles) collected charges for -5 V (left) and -90 V (right).

CHAPTER V

PULSED LASER RESULTS: EXPERIMENTAL RESULTS, SENSITIVE VOLUMES, AND SIMULATIONS

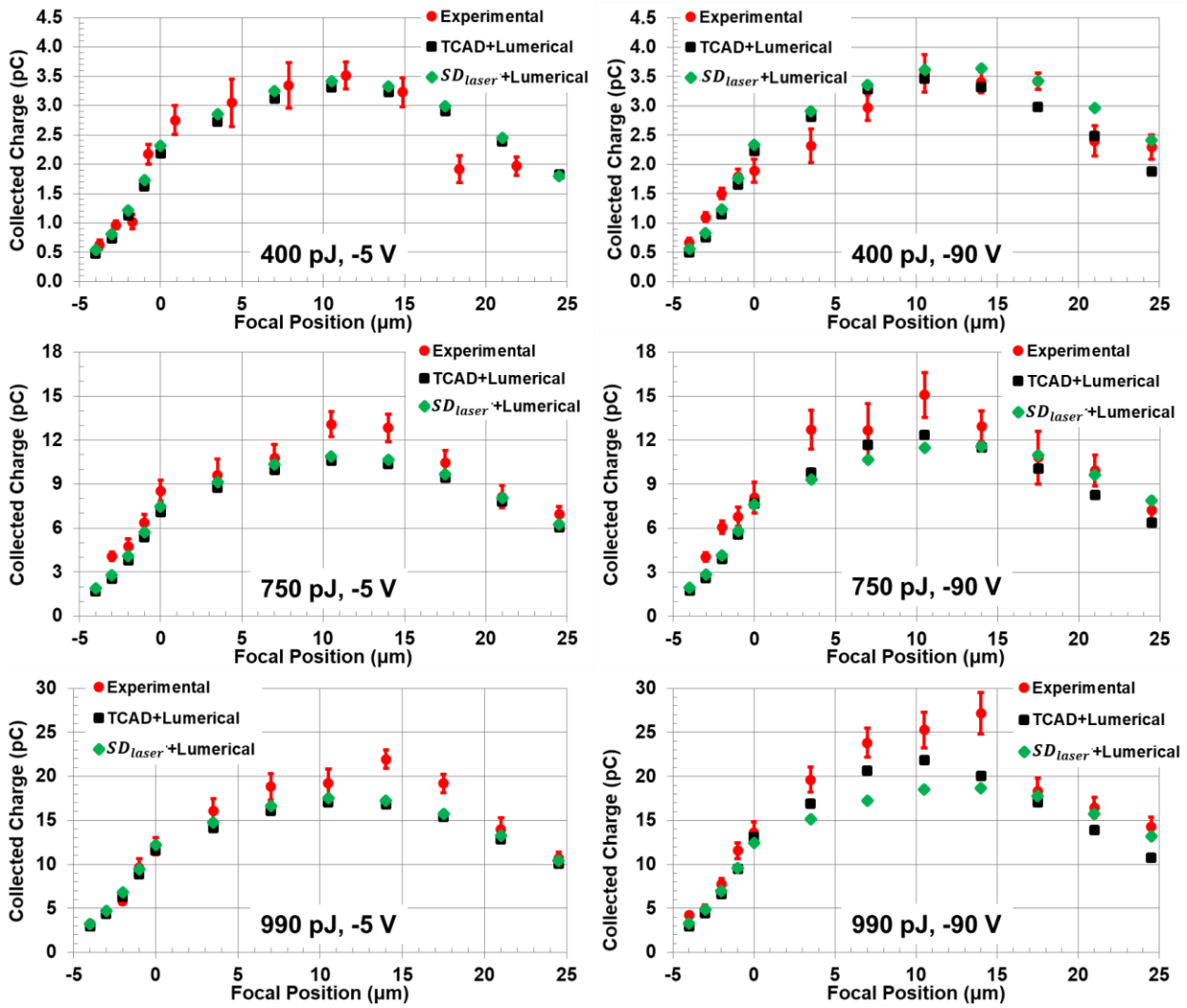

Figure V. 1. Laser-induced collected charge for -5 V (left) and -90 V (right) at pulsed energies of 400 pJ (top), 750 pJ (middle), and 990 pJ (bottom). Experimental results are shown as red circles with error bars of one standard deviation from 200 SETs. TCAD simulated collected charge is shown as black squares, and sensitive volume predictions are given as green diamonds.

Experimental laser-induced collected charge as a function of laser focal position is shown in Figure V.1. Results are shown for pulsed energies of 400 pJ, 750 pJ, and 990 pJ and for biases of -5 V and -90 V. The error bars show one standard deviation from the mean given 200 SETs. For each focal position a Lumerical time-integrated charge generated distribution, such as those

shown in Figure II.3, were created using the appropriate pulsed energy and parameters given in Section III.2. These charge distributions were ported into Sentaurus TCAD for 2D cylindrical mixed-mode transient simulations. Figure III.2 shows the device deck used in these simulations. Doping profiles were determined by spreading resistance measurements and read in from a file, and the width of the diode was set so the cylindrical area is equal to the actual area of the diode. Figure III.3 shows the circuit diagram used in the simulations, with the bias tees and oscilloscope connections being modeled by their equivalent circuits. Transients were monitored off of node N2, which is equivalent to the front end of the oscilloscope in experiments. The collected charge from these simulations is shown as black squares in Figure V.1 and shows good agreement with the experimental results.

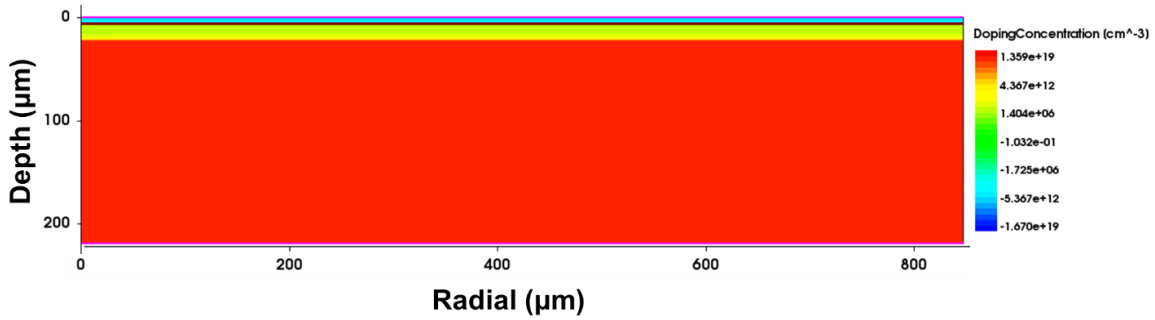

Figure V. 2. Cross section of the diode structure used for Sentaurus TCAD simulations. The doping profile was read in from a file containing spreading resistance measurements of the diode. The radial dimension was chosen so that the cylindrical area of the TCAD deck is the same as the experimental area.

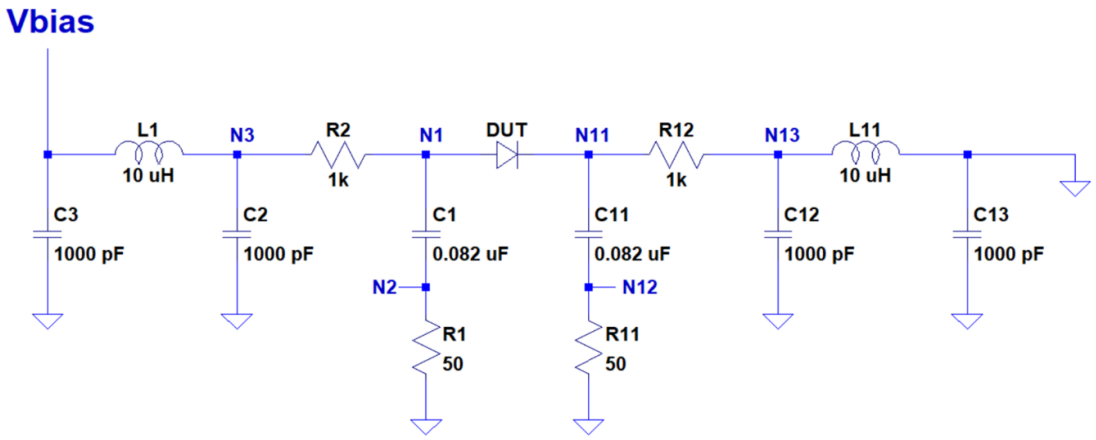

Figure V. 3. Circuit diagram of the mixed model used to capture the effect of experimental setup. The 50 Ω resistors are used to model the 50 Ω impedance on the oscilloscopes, and nodes N2 and N12 are used for analysis.

A sensitive volume depth defined from laser-induced charge collection, SD_{laser}, was found using the most deeply focused position at the highest pulse energy: 24 μm focal position at 990 pJ. The Gaussian shape of the generated charge distributions allows the most deeply focused position to be used because the sensitive volume depths at the less deeply focused positions will be encompassed by the sensitive volume depth at the most deeply focused position. The highest pulsed energy was used because nonlinear effects are more prevalent at higher pulse energies. SD_{laser} was found to be 23 μm and 26 μm for -5 V and -90 V, respectively. SD_{laser} was then used to predict the collected charge for the other focal positions and pulsed energies. These results are shown as green diamonds in Figure V.1. Overall, the single SD_{laser} for each bias condition exhibits good agreement with the TCAD and experimental results across all focal positions and pulsed energies.

CHAPTER VI

COMPARISON OF ION- AND LASER-INDUCED SENSITIVE VOLUMES

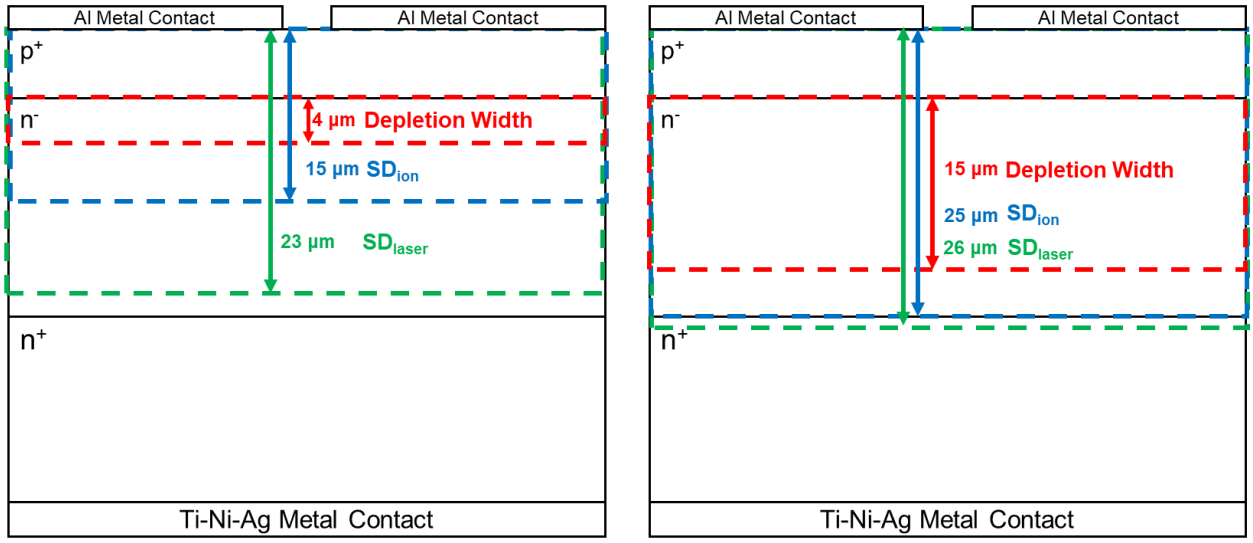

Figure VI. 1. Graphical comparison of ion- and laser-based sensitive volumes with the depletion widths at -5 V (left) and -90 V (right). When the diode is fully depleted, as seen at -90 V, the sensitive volumes are the same. Otherwise, they appear to be different due to different amount of potential modulation.

Figure VI.1 is a visual comparison of the ion- and laser-based sensitive volumes found for both bias conditions and provides insights on possible mechanisms for the differences seen. At the lower bias the laser-based sensitive volume is 8 µm larger than the ion-based sensitive volume. At the higher bias the epi-layer is close to being fully depleted and modulation of the depletion region for both the ion- and laser-induced charge is truncated by the heavily doped substrate. As such, there is only a 1 µm difference between the two sensitive volumes.

The differences in the sensitive volumes at -5 V are most likely due to differences in potential modulation from high carrier injection. Recall that the laser-based sensitive volume is found using the collected charge from the focal position with the most deeply deposited charge. The majority of the carriers are being generated well outside the depletion region and yet still contribute to potential modulation. The charge generated outside of the depletion region diffuses up towards the depletion region and then causes an extended modulation region, resulting in the larger sensitive

volume. This is supported by the similar sensitive volumes seen between the -5 V and -90 V laser-based sensitive volumes.

A hope for laser-induced SEE testing is the ability to predict ion-induced SEEs. If the sensitive volumes differ, however, this may not be possible without first empirically correlating the ion- and laser-induced responses. For example, Figure VI.2 shows the collected charge from the ion experiments, along with the charge that would be predicted using either SD_{ion} or SD_{laser} for the appropriate bias in Equation II. While the ion-based sensitive volume shows good agreement with experimental results within 15%, the laser-based sensitive volume over predicts the collected charge by upwards of 75% for -5 V. The -90 V results are as expected, with both ion- and laser-based sensitive volumes predicting the collected charge within 10% of the experimental values. Figure VI.3 shows an analogous comparison using SD_{ion} to attempt to predict laser-induced collected charge. SD_{ion} under predicts the laser-induced collected at the low bias condition and is consistent with SD_{laser} at the higher bias condition. If the sensitive volumes are similar then the predicted collected charges will be similar.

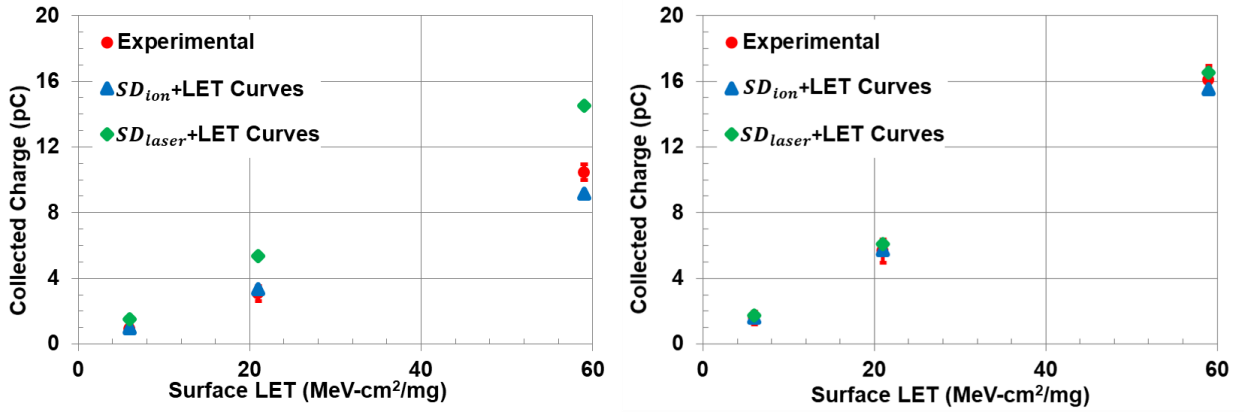

Figure VI. 2. Comparison of experimental (red circles), ion-based sensitive volume predicted (blue triangles), and laser-based sensitive volume predicted (green diamonds) collected charge for -5 V (left) and -90 V (right) biases.

Differing error rate predictions is another ramification of differing sensitive volumes. The sensitive volumes were put into CRÈME96 [5], [6], [24] to explore the effects of the differing sensitive volumes. An error rate based on the ISS orbit and current space weather conditions was calculated in CRÈME96 assuming a critical charge of 0.5 pC, the lowest collected charge experimentally observed. Table VI.1 gives the error rates calculated for both the ion- and laser-based sensitive volumes. The laser-based error rate is over 2 times higher than the ion-based

error rate at -5 V, while at -90 V the error rate are nearly identical. This is consistent with the trends seen in the predicted collected charge.

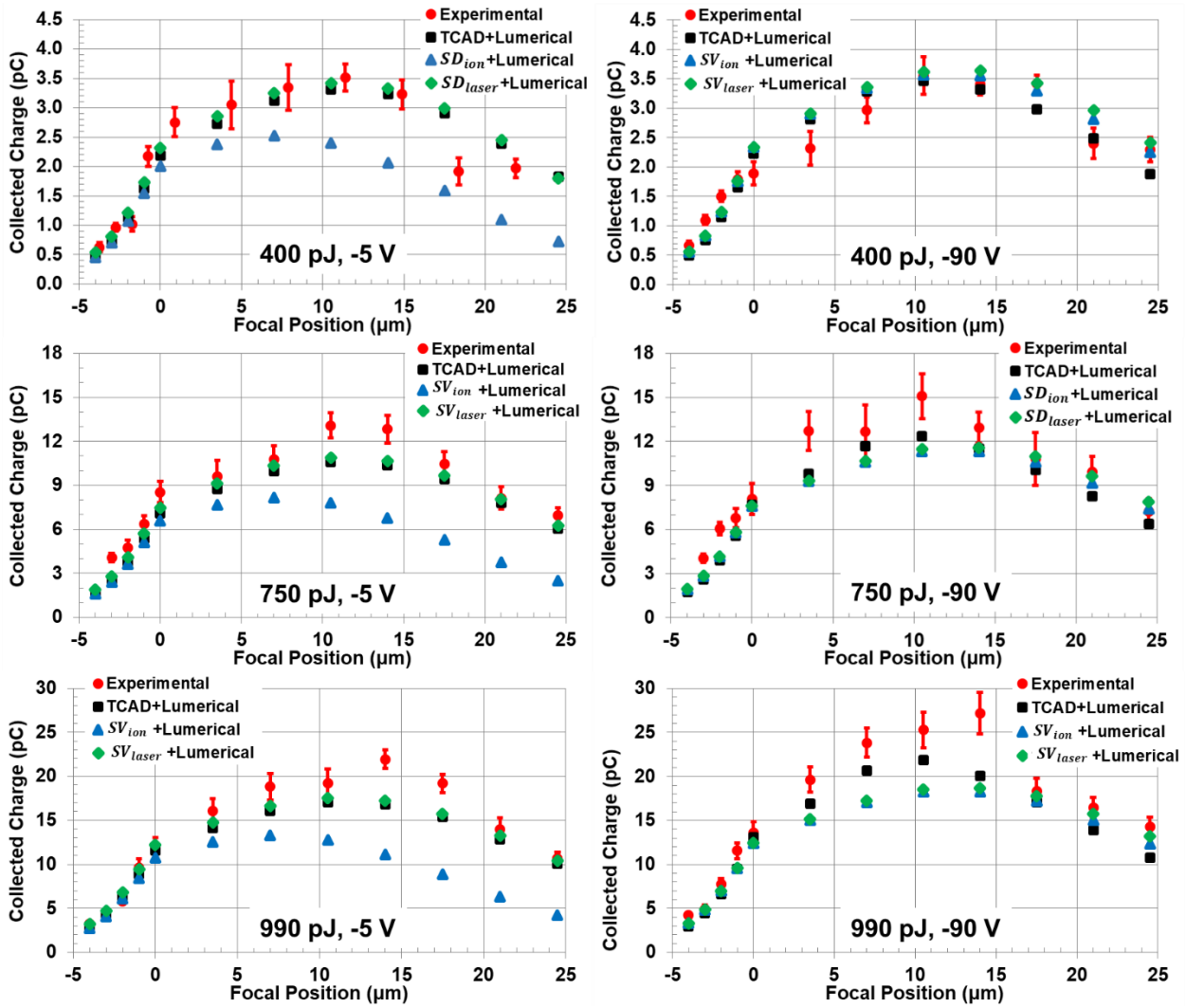

Figure VI. 3. Comparison of experimental (red circles), TCAD simulated (black squares), ion-based sensitive volume predicted (blue triangles), and laser-based sensitive volume predicted (green diamonds) collected charge for the pulsed laser experiments.

TABLE VI.2 ERROR RATE PREDICTIONS

Source	Bias (V)	Error Rate (SEEs·sec^{-1})
Ion	-5	2.3×10^{-4}
Laser	-5	5.3×10^{-4}
Ion	-90	6.3×10^{-4}
Laser	-90	6.8×10^{-4}

CHAPTER VII

CONCLUSIONS

This work aimed at comparing the sensitive volumes found from heavy ion- and pulsed laser-induced SEE experiments. Sensitive volumes were found using experimentally determined collected charge for two different bias conditions, -5 V and -90 V. LET curves were used to calculate the amount of deposited charge from ions and time-integrated charge generated distributions from Lumerical were used for laser-deposited charge. The generated charge was then integrated over until it was equal to the experimental collected charge, and the path length was defined as the sensitive volume depth. The ion- and laser-based sensitive volumes were used to predict the collected charge from their respective charge deposition methods and were found to show good agreement with the experimental results. When compared, the ion- and laser-based sensitive volumes at -5 V were found to be different by 8 μm, while the -90 V sensitive volumes only differed by 1 μm. The 8 μm difference seen at -5 V results in the laser-based sensitive volume over predicting the amount of collected charge observed by heavy ions by as much as 71% and an error rate over twice as high. The 1 μm difference between -90 V sensitive volumes results in negligible differences between the predicted collected charge and error rates.

From this work, it is clear that a direct comparison of ion- and laser-based SEEs is not a straight forward path to relating these two charge deposition methods. The sensitive volumes differ at the lower bias condition, when the device is not fully depleted. When the device is fully depleted, the sensitive volumes are nearly identical. This suggests that the ion- and laser-deposited charge are modulating the internal potential differently and this effect is masked when potential modulation is truncated by the heavily-doped substrate. Understanding the physical mechanisms behind the differences seen here will allow for a path forward to relating ion- and laser-based SEEs and how the pulsed laser can best be used in SEE investigations.

REFERENCES

[1] J. C. Pickel and J. T. Blandford Jr., “Cosmic ray induced errors in MOS memory cells,” *IEEE Trans. Nucl. Sci.*, vol. NS-25, p. 1166, 1978.

[2] E. L. Petersen, “Predictions and observations of SEU rates in space,” *IEEE Trans. Nucl. Sci.*, vol. 44, p. 2174, 1997.

[3] B. D. Sierawski, J. A. Pellish, R. A. Reed, R. D. Schrimpf, K. M. Warren, R. A. Weller, M. H. Mendenhall, J. D. Black, A. D. Tipton, M. A. Xapsos, R. C. Baumann, X. Deng, M. J. Campola, M. R. Friendlich, H. S. Kim, A. M. Phan, and C. M. Seidleck, "Impact of Low-Energy Proton Induced Upsets on Test Methods and Rate Predictions," *IEEE Trans. Nucl. Sci.*, vol. 56, pp. 3085-3092, Dec. 2009.

[4] K. M. Warren, R. A. Weller, B. D. Sierawski, R. A. Reed, M. H. Mendenhall, R. D. Schrimpf, L. W. Massengill, M. E. Porter, J. D. Wilkinson, K. A. LaBel, and J. H. Adams, "Application of RADSAFE to Model the Single Event Upset Response of a 0.25 um CMOS SRAM," *IEEE Trans. Nucl. Sci.*, vol. 54, pp. 898-903, Aug. 2007.

[5] A. J. Tylka, J. H. Adams, Jr., P. R. Boberg, B. Brownstein, W. F. Dietrich, E. O. Flueckiger, E. L. Petersen, M. A. Shea, D. F. Smart, and E. C. Smith, "CREME96: A Revision of the Cosmic Ray Effects on Micro-Electronics Code," *IEEE Trans. Nucl. Sci.*, vol. 4, pp. 2150-2160, Dec. 1997.

[6] Marcus H. Mendenhall and Robert A. Weller, "A probability-conserving cross-section biasing mechanism for variance reduction in Monte Carlo particle transport calculations", *Nucl. Inst. & Meth. A*, Volume 667, 1 March 2012, Pages 38-43, doi:10.1016/j.nima.2.

[7] D. McMorrow, W. T. Lotshaw, J. S. Melinger, S. Buchner, Y. Boulghassoul, L. W. Massengill, and R. L. Pease, "Three-Dimensional Mapping of Single-Event Effects Using Two Photon Absorption," *IEEE Trans. Nucl. Sci.*, vol. 50, no. 6, pp. 2199-2207, Dec. 2003.

[8] S. P. Buchner, F. Miller, V. Pouget, and D. P. McMorrow, "Pulsed-Laser Testing for Single-Event Effects Investigations," *IEEE Trans. Nucl. Sci.*, vol. 60, no. 3, pp. 1852-1875, June 2013.

[9] A. Khachatrian, N. J. Roche, S. P. Buchner, A. D. Koehler, J. D. Greenlee, T. J. Anderson, J. H. Warner, and D. McMorrow, "Spatial Mapping of Pristine and Irradiates AlGaN/GaN HEMTs with UV Single-Photon Absorption Single-Event Transient Technique," *IEEE Trans. Nucl. Sci.*, vol. 63, no. 4, pp. 1995-2001, 2016.

[10] J. M. Hales, N. J. Roche, A. Khachatrian, D. McMorrow, S. Buchner, J. Warner, M. Turowski, K. Lilja, N. C. Hooten, E. Zhang, R. A. Reed, and R. D. Schrimpf, "Strong Correlation Between Experiment and Simulation for Two-Photon Absorption Induced Carrier Generation," *IEEE Trans. Nucl. Sci.*, vol. 64, pp. 1133-1136, May 2017.

[11] J. M. Hales, A. Khachatrian, S. Buchner, N. J. Roche, J. Warner, and D. McMorrow, "A Simplified Approach for Predicting Pulsed-Laser-Induced Carrier Generation in Semiconductors," *IEEE Trans. Nucl. Sci.*, vol. 64, no. 3, pp. 1006-1013, Mar. 2017.

[12] Z. E. Fleetwood, N. E. Lourenco, A. Ildefonso, J. H. Warner, M. T. Wachter, J. M. Hales, G. N. Tzintzarov, N. J. Roche, A. Khachatrian, S. P. Buchner, D. McMorrow, P. Paki, and J. D. Cressler, "Using TCAD Modeling to Compare Heavy-Ion and Laser-Induced Single Event Transients in SiGe HBTs," *IEEE Trans. Nucl. Sci.*, vol. 64, no. 1, pp. 398-405, Jan. 2017.

[13] A. Ildefonso, Z. E. Fleetwood, G. N. Tzintzarov, J. M. Hales, D. Nergui, M. Froumchi, A. Khachatrian, S. P. Buchner, D. McMorrow, J. H. Warner, J. Harms, A. Erickson, K. Voss, V. Ferlet Cavrois, and J. D. Cressler, "Optimizing Optical Parameters to Facilitate Correlation of Laser- and Heavy-Ion-Induced Single-Event Transients in SiGe HBTs," *IEEE Trans. Nucl. Sci.*, vol. 66, pp. 359-367, Jan. 2019

[14] J. M. Hales, A. Khachatrian, S. Bucnher, N. J. Roche, J. Warner, Z. E. Fleetwood, A. Ildefonso, J. D. Cressler, V. Ferlet Cavrois, and D. McMorrow, "Experimental Validation of an Equivalent LET Approach for Correlating Heavy-Ion and Laser-Induced Charge Deposition," *IEEE Trans. Nucl. Sci.*, vol. 65, pp. 1724-1733, Aug. 2018.

[15] J. F. Ziegler, SRIM - The Stopping and Range of Ions in Matter.

[16] J. M. Trippe, R. A. Reed, R. A. Austin, B. D. Sierawski, L. W. Massengill, R. A. Weller, B. Bartz, and D. Reed, "Predicting Muon-Induced SEU Rates for a 28-nm SRAM Using Protons and Heavy Ions to Calibrate the Sensitive Volume Model," *IEEE Trans. Nucl. Sci.*, vol. 65, pp. 712-718, Feb. 2018.

[17] N. C. Hooten et al., "The Signficance of High-Level Carrier Generation Conditions for Charge Collection in Irradiated Devices," *IEEE Trans. Nucl. Sci.*, vol. 59, pp. 2710-2721, Dec. 2012.

[18] Lumerical. FDTD Solutions. Accessed: Apr. 2017. [Online]. Available: https://www.lumerical.com/tcad-products/fdtd/.

[19] L. D. Ryder, "Simulation of Optical Energy Deposition for Pulsed Laser-Induced Single Event Effects Testing in Microelectronic Devices," M.S. thesis, Dept. of Elect. Eng. and Comp. Sci., Vanderbilt University, Nashville, TN, 2019.

[20] I. K. Samsel, E. Zhang, N. C. Hotten, E. D. Funkhouser, W. G. Bennett, R. A. Reed, R. D. Schrimpf, M. W. McCurdy, D. M. Fleetwoood, R. A. Weller, G. Vizkelethy, X. Sun, T. Ma, O. I. Saadat, and T. Palacios, "Charge Collection Mechanisms in AlGaN/GaN Mos High Electron Mobility Transistors," *IEEE Trans. Nucl. Sci.*, vol. 60, pp. 4439-4445, Dec. 2013.

[21] J. A. Pellish, R. A. Reed, D. McMorrow, G. Vizkelethy, V. F. Cavrois, J. Baggio, P. Paillet, O. Duhamel, K. A. Moen, S. D. Phillips, R. M. Diestelhorst, J. D. Cressler, A. K. Sutton, A. Raman, M. Turowski, P. E Dodd, M. L. Alles, R. D. Schrimpf, P. W. Marshall, and K. A. Label, "Heavy ion microbeam- and broadbeam-induced transients in SiGe HBTs," *IEEE Trans. Nucl. Sci.*, vol. 56, no. 6, pp. 3078–3084, Dec. 2009.

[22] M. B. Johnson. Cocktails and Ions [Online]. Available FTP: http://cyclotron.lbl.gov/base-rad-effects/heavy-ions/cocktails-and-ions.

[23] A. Khachatrian, N. J. Roche, D. McMorrow, J. H. Warner, S. P. Buchner, and J. S. Melinger, "A Dosimetry Methodology for Two-Photon Absorption Induced Single-Event Effects Measurements," *IEEE Trans. Nucl. Sci.*, vol. 61, pp. 3416-3423, Dec. 2014.

[24] R.A. Weller, M. H. Mendenhall, R. A.Reed, R. D. Schrimpf, K. M. Warren, B. D. Sierawski, and L. W. Massengill, "Monte carlo simulation of single event effects," *IEEE Trans. Nucl. Sci.*, vol. 57, no. 4, pp. 1726-1746, Aug. 2010.